Doping induced structural changes in colloidal semiconductor nanowires

Krishna Prasad Kandel,[a] Ullrich Pietsch,[a] Zhen Li*[b] and Özgül Kurtulus Öztürk*[c]

Undoped and Mn^{2+}-doped CdSe nanowires (NWs) grown by a solution–liquid–solid (SLS) method using Bi nanocatalysts have been studied by X-ray powder diffraction measurements. Except for heavily doped nanowires no measurable changes in nanowire lattice parameters were observed. The lattice parameter of heavily doped nanowires shrinks by about 0.5% compared with the undoped ones, which corresponds to a doping concentration of 1.6%. For the other samples no change in lattice parameter is measured referring to a doping level much below 1%. Real structural parameters of nanowires were found to vary as a function of doping level, such as the zinc blende to wurtzite ratio, the static Debye–Waller factor, axial strain, and the number of stacking faults. Compared with the undoped nanowires the overall perfection is slightly improved for low doping but deteriorates drastically for higher doping. Our results highlight the importance of controlling the dopant concentration during the preparation of doped nanostructures.

Introduction

Low dimensional crystalline semiconductor nanostructures with sizes ranging from a few nanometers to micrometers have been attractive due to their unique optical, electrical, mechanical, and chemical properties which cannot be found in thin film and bulk materials. Research studies are particularly focused on one-dimensional semiconductor nanowires (NWs) because of their size tunable electrical, optical and thermoelectric characteristics.[1–3] They can grow to long lengths with their diameters limited in a quantization size which results in quantum confinement effect.

Doping can alter the physical properties of semiconductor nanostructures in controllable and desirable ways, and it can be done by wet-chemical and non-wet chemical approaches. For example, electron- and hole-doping performed in the vapor phase can significantly improve semiconductor conductivity and their device performance, demonstrated by field-effect transistors fabricated from p-type or n-type Si nanowires.[4–7] In addition to electron- and hole-doping, paramagnetic doping has become more attractive because paramagnetic-ion-doped semiconductor nanostructures such as dots, rods, wires and films exhibit fascinating properties and potential applications in solar cells,[8] bioimaging,[9,10] spintronics[11] and quantum interference information processing.[11] Doping can change nanomaterial structural parameters as well as properties. For example, in solar cells doping may protect the material against photo-oxidation,[12] for a magnetic material the doping enhances the quantum mechanical spins in the nanocrystal.[13] Therefore, the structural study of doped nanomaterials is a crucial issue not only for understanding their novel properties, but also for applying them in different areas.

Cadmium selenide (CdSe) is a II–IV semiconductor material with a direct energy band-gap of 1.74 eV at room temperature, and its nanostructures have been extensively investigated due to their unique properties and diverse applications ranging from biomarkers to optic-electronic devices.[9,14] For example, undoped CdSe NWs prepared by the solution–liquid–solid (SLS) approach exhibit the photoluminescence heterogeneity[15,16] in individual wires and the doped analogues show the anti Varshni-like temperature dependence of photoluminescence.[17] Their photoluminescence can be improved by building a core–shell structure.[18] Although the exact mechanisms for these novel properties are unclear, the change in nanowire crystal and electronic structure[19] is considered to be responsible. This work presents the structural investigation of one dimensional magnetically active[11,12,20] Mn^{2+}-doped CdSe NWs by means of the X-ray diffraction technique. Due to the special route of sample preparation, nanowire ensembles can be inspected using powder diffraction. The mean structural parameters such

[a] *Department of Physics, University of Siegen, 57068 Siegen, Germany*
[b] *Institute for Superconducting and Electronic Materials, The University of Wollongong, NSW 2500, Australia. E-mail: zhenl@uow.edu.au; Fax: +61-2-42215731; Tel: +61-2-42215163*
[c] *Department of Physics, Dogus University, 34722 Istanbul, Turkey. E-mail: okurtulus@dogus.edu.tr*

4444 | *Phys. Chem. Chem. Phys.*, 2013, **15**, 4444–4450

This journal is © the Owner Societies 2013

as lattice parameter, static Debye Waller factor, size of coherently scattered units within the nanowire and residual strains can be obtained. In addition, the ratio between wurtzite and zinc blende structure phase units and the influence of stacking faults (SFs) on the NW structure is estimated. The mean SF arrangement within the NW has been estimated by curve simulations using the DISCUS code.[21] The results show that doping could improve or deteriorate nanowire crystallinity, depending on the dopant concentration. This demonstrates the importance of controlling the dopant concentration when dopants are incorporated intentionally into nanostructures in order to induce novel properties and functions.

Experimental methods

Synthesis

One undoped and three Mn^{2+}-doped samples with different doping levels were synthesized by the SLS method.[22–26] They are marked as CdSe (sample A), 0.25 Mn–CdSe (sample B), 1.0 Mn–CdSe (sample C), 2.0 Mn–CdSe (sample D), corresponding to the relative volume of MnSe nanoclusters (measured in mL) used in the synthesis of doped samples (see Table 1).

Undoped CdSe NWs have been described elsewhere,[25] and doped analogues were synthesized using MnSe nanoclusters[27] as precursors. The MnSe nanoclusters were prepared as follows: 2.45 g manganese stearate was dissolved in 20 mL octylether in the presence of 2.0 mL trioctylphosphine (TOP) and then mixed with 2.0 mL TOPSe (2.0 mol L^{-1}). The reaction of the mixture took place for 3 h at 100 °C under 1 mbar. The colourless solution gradually turned brown, indicating the formation of MnSe nanoclusters. Then the flask was filled with argon and the temperature was increased to 150 °C, and kept for 1 h. The MnSe cluster solution was cooled and stored in a glove box (H_2O < 1 ppm) for further use.

As a next step, 3.0 g TOPO, 24.7 mg CdO and 0.23 mL octanoic acid were loaded in a 50 mL three necked flask connected with a reflux condenser and a standard Schlenk line. The mixture was dried and degassed for 30 min at 100 °C under vacuum. After the flask was filled back with argon, the temperature was increased to 330 °C resulting in a clear solution, and kept for 30 min. Then a mixture of Bi nanoparticles (100 µL, 3.63 mM) and as-synthesized MnSe solution (varied from 0.25 mL to 2.0 mL) was quickly injected into the Cd-precursor solution at 330 °C. The solution reacted for 1 min and then cooled to 80 °C, followed by the addition of 2 mL

toluene to prevent the TOPO from solidifying. The resultant NWs were separated from the solution through high speed centrifugation (14 800 rpm, 10 min) and washed with toluene several times. The purified NWs were re-dispersed in chloroform for characterization. This route can produce NWs with lengths in the order of micrometers and diameters in the order of 10 nm.

Characterizations

TEM images were recorded on a JEOL 1011 instrument operating at a voltage of 100 kV after deposition of diluted NW solution onto a 400 mesh copper grid. HRTEM images were collected on a JEOL 2100 microscope operating at an acceleration voltage of 200 kV. The overall dopant concentration was determined using inductively-coupled-plasma mass spectrometry (ICP-MS).
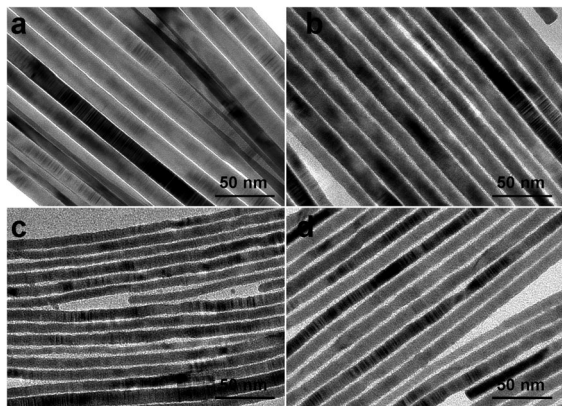
Due to the particular shape of NW samples, standard high-resolution X-ray diffraction techniques cannot be applied to a single wire for detailed structure analysis.[28–30] Therefore X-ray powder diffraction has been used for structure investigation of as-synthesized CdSe NWs to provide averaging information. The measurements of samples B–D were performed at the beamline P08 of PETRA III storage ring (Hamburg) using a photon energy of 25 keV and a beam size of 1.0×0.5 mm^2 (horizontal × vertical). The CCD detector used has 4096×4096 pixels with pixel size of 15×15 µm^2. The distance between the sample and the CCD detector was 77 cm. For the measurements, the NW powders were loaded in between two capton foils and mounted at the centre of the Kohzu high precision 6-circle diffractometer. The CCD images taken in transmission geometry show a ring-like structure without major texture. Due to the limited aperture of the detector a sector of the full powder pattern was recorded by taking subsequent images at different mean scattering angles 2θ scanning in steps of 4.6°. The patterns were corrected by a flat field, background and radial line scans were extracted by azimuth averaging the Debye–Scherrer rings using the software Fit2D. The data of sample A were taken at DELTA Synchrotron (TU Dortmund) at 15.5 keV. For details see ref. 25.

Results and discussion

The SLS method is capable of producing dispersible semiconductor nanowires with tunable sizes. Under an optical microscope the resultant NWs look like a ball of wool. Many micron long but thin wires are mutually interpenetrating and show only small area of straight sections with preferential orientation. Fig. 1 shows the TEM images of undoped and Mn^{2+}-doped CdSe NWs. The surface of undoped NWs (sample A) appears to be smoother than that of other doped samples (B–D). From TEM images the average diameters were found to be 15.1 nm, 12.2 nm, 8.3 nm, and 10.1 nm for samples A–D with a standard deviation of about ±1.5 nm as listed in Table 1. The bigger size of sample D compared to sample C could be due to the complicated competitive reactions in the SLS system. There are at least three parallel reactions happening during the SLS

Table 1 Lattice parameters and ZB content of undoped and Mn^{2+}-doped CdSe nanowires

Sample	Diameter (nm)	Lattice a(Å) ±0.0047	Lattice c(Å) ±0.0052	ZB content (%)	Static DWF (Å)
A	15.1	4.2936	7.0175	5	0
B	12.2	4.2936	7.0175	8	0.02
C	8.3	4.2936	7.0175	12	0.03
D	10.1	4.2737	6.9799	75	0.14
Theoretical value		4.299	7.010		

This journal is © the Owner Societies 2013

Phys. Chem. Chem. Phys., 2013, **15**, 4444–4450 | **4445**

Fig. 1 TEM images of undoped and Mn^{2+}-doped CdSe NWs: (a) undoped sample; (b–d) doped samples with a dopant concentration of 0.6%, 1.5% and 2.6%, respectively.

growth, *i.e.* the catalytic growth of nanowires, the uncatalytic growth of nanocrystals and the growth of catalysts.[25] In addition, the doping process is in contradiction with the crystal self-purification process,[31] which makes these reactions more complicated.

The different brightness within the same NW seen in all images may indicate the changes in facet orientation or structural phase,[32,33] due to the small energy difference between the hexagonal wurtzite (W) phase and the cubic zinc-blende (ZB) phase (the offsets for conduction bands and valence bands are 76–144 meV and 30–59 meV, respectively).[34] In addition SFs are visible. In order to investigate the heterogeneity of crystal structure in NWs, HRTEM images were taken and Fig. 2 shows the typical images for samples C and D. They clearly display the crystal heterogeneity in individual nanowires, *i.e.* the alternation of W and ZB structure, and the twins. The lattice fringes with a spacing of about 0.35 nm on an average correspond to the (002) or (111) lattice spacing of hexagonal or cubic CdSe.

In order to quantify the ratio of W and ZB, X-ray diffraction patterns of all samples are extracted from CCD images and plotted as a function of q as shown in Fig. 3 using $q = 4\pi\sin\theta/\lambda$, where λ is the wavelength and θ is the scattering angle. They provide structural information averaged over the illuminated sample volume. All the peaks visible in the diffraction patterns are indexed by the Miller indices of either W or ZB structure. Most of the expressed Bragg peaks reveal an admixture of W and ZB reflections,[25,32] which is consistent with the HRTEM results. Compared to the other reflections the 002W/111ZB reflection is the most intense because it is a measure of the stacking of hexagonally dense packed CdSe bilayers along the NW length axis. Except for sample D, Bragg peaks are visible up to about $q_{max} \approx 6.5$ Å^{-1} corresponding to a spatial resolution of about 1.1 Å. For sample D the intensity is very low and the degeneracy of peaks is so strong that no peak could be determined beyond the 112W/311ZB one ($q_{max} \approx 3.5$ Å^{-1}).

The overall intensity of reflections is mainly affected by the amount of NW material used for measurement and their packing density. So the amount of material for sample D was
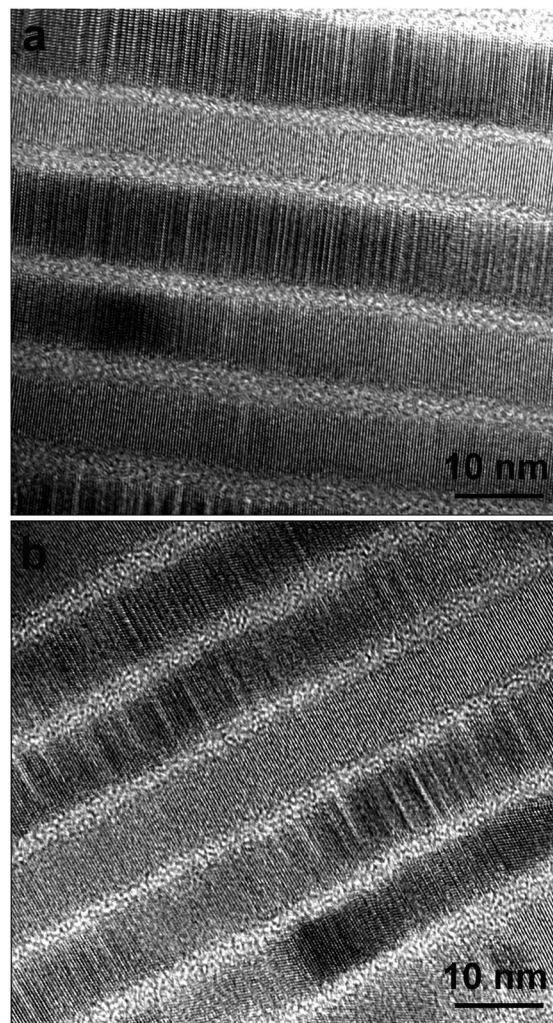
Fig. 2 HRTEM images of Mn^{2+}-doped CdSe NWs showing the heterogeneity of crystal structure.
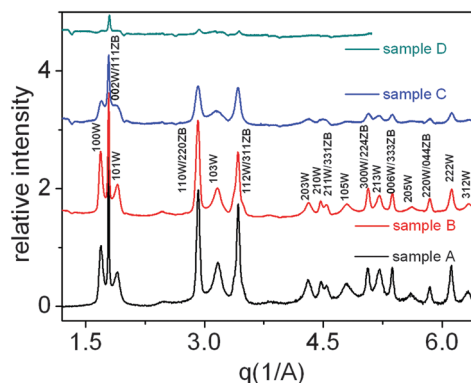
Fig. 3 X-ray diffraction patterns of undoped (sample A) and Mn^{2+}-doped CdSe NWs (samples B–D).

very small explaining the low intensity. However, when compared on a relative scale samples A and B show same peaks with almost similar peak intensities and similar intensity ratios

between W and ZB reflections up to $q = q_{max}$, whereas the peak intensity of sample C is already reduced by a factor of two. A major drop in the intensity ratio for increasing q is attributed to the faster decrease of W reflections than ZB ones, demonstrated by 100W and 103W.

Structure and lattice parameters can be determined from the angular positions of Bragg peaks. This was done in terms of the hexagonal lattice where the q-space is related to lattice parameters as in eqn (1):

$$q = \frac{2\pi}{d_{hkl}} = \frac{2\pi}{a_{hex}}\sqrt{\frac{4}{3}(h^2 + k^2 + hk) + \frac{a_{hex}^2}{c_{hex}^2}l^2} \qquad (1)$$

where a_{hex} and c_{hex} are the lattice parameters. The lattice constant a_{hex} is evaluated using lattice planes indexed with Miller index $l = 0$ (in-plane reflections) and c_{hex} is obtained mainly from out of plane reflections like $00l$. The calculated and theoretical lattice parameters are summarized in Table 1. Within the experimental errors the lattice parameters a and c of samples A, B and C are the same and in agreement with literature values, but they show a small reduction by less than 0.5% for sample D. Due to the smaller ionic radius of Mn^{2+} compared to Cd^{2+}, a reduction in the lattice parameter is expected after Mn^{2+}-doping into the CdSe lattice.[26,35] Using Vegard's law and both radii, the measured lattice reduction of sample D refers to a Mn^{2+} concentration of about 1.6%. Subsequently the Mn^{2+} concentration of samples B and C has to be much below 1%. The calculated dopant concentration is smaller than that determined by the ICP-MS, which could be due to the unsuitability of Vegard's law at very low dopant concentrations, or some Mn-species adsorbed on the surface of nanowires despite being thoroughly washed with toluene and chloroform.

The intensity of Bragg reflections depends on the square of the structure factor, $F(hkl)$, of the respective Bragg reflection damped by a thermal and static Debye Waller factor (DWF). The mean ratio between ZB and W structural units within the NW can be estimated comparing the scattering intensities of ZB and W phase Bragg reflections. In particular the intensity of the pure (100)W Bragg peak and the mixed (002W/111ZB) peak are compared using the theoretical structure factors of both W and ZB, F_{WZ} and F_{ZB}, respectively. Details of the calculation have been described elsewhere.[32] Geometric factors and the influence of thermal Debye–Waller factors are neglected as the q-values of both reflections are very close to each other. As shown in Table 1 the ZB structure content within the NWs increases by increasing the doping concentration. Whereas it is 5% for the undoped sample it increases to 8%, 12% and finally 75% for samples B, C and D, indicating that the NW growing process becomes in favor of the ZB phase under the influence of Mn^{2+} doping, which is the most prominent for sample D.

One of the main features seen in Fig. 3 is the drop in Bragg peak intensities for increasing q-value. One can expect that the inclusion of Mn^{2+} within the CdSe lattice generates a certain static displacement of the host atoms out of their positions. Substitution of Cd^{2+} by Mn^{2+} will locally change the tetrahedral
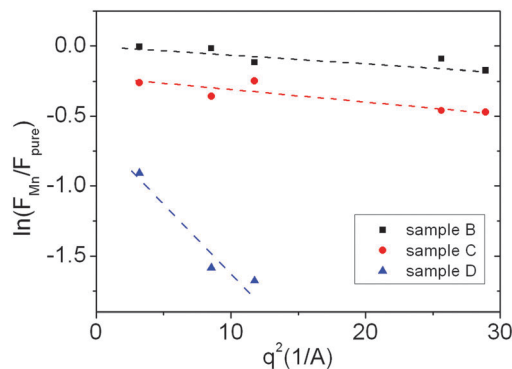

Fig. 4 Static displacement factors of Mn^{2+}-doped CdSe NWs.

coordination originating a certain strain field in the further neighborhood. On an average, these displacements appear random and reduce the X-ray structure factor. Considering the concept of static DWF, the scattering factor is damped with increasing q value by a Gaussian with a damping factor, B_s. The latter can be determined by applying eqn (2):

$$\ln\left(\frac{F_{Mn}}{F_{pure}}\right) = -B_s q^2 \qquad (2)$$

where F_{Mn} is the structure factor of Mn^{2+}-doped NWs and F_{pure} is that of the undoped NWs. Fig. 4 shows the relation for selected Bragg reflections as a function of q^2 for samples B, C and D. Following eqn (2) B_s is determined to be 0.0018 Å^2, 0.0035 Å^2 and 0.094 Å^2 for samples B, C and D respectively. Considering $B_s = 4\pi/3 \langle u_s^2 \rangle$ the static displacement $\sqrt{\langle u_s^2 \rangle}$ is calculated as 0.02 Å, 0.03 Å and 0.14 Å, respectively, as listed in Table 1. The large damping factor found for sample D refers to the appearance of interstitials and defect clusters caused by the large amount of dopants.

Next the peak widths are investigated. The suggested admixture of ZB and W structural units within the same NW is accompanied by the inclusion of stacking faults (SF). According to Warren's report, Bragg peaks with $h - k = 3n \pm 1$ (n is ordinary number) experience peak broadening due to the impact of faults.[32,36] Alternatively reflections of the class $h - k = 3n$ are not affected by SFs and can be independently used for the determination of grain size, D and residual strain. With varying phase composition D is a measure for the length of coherently scattering units within a NW, i.e. units of perfect stacking, also expressed by the quantity coherence length. The peak width might be additionally increased by the impact of strain ε, where this strain changes as a function of Bragg angle θ. Both quantities can be separated by the Williamson–Hall plot.[37] For quantitative analysis the shape of Bragg peaks are approximated by Gaussians and the FWHM, $\Delta_{2\Theta}$, can be expressed by eqn (3):[38,39]

$$\Delta_{2\Theta} = \frac{k\lambda}{D\cos\theta} + \varepsilon\tan\theta \qquad (3)$$

where $k \approx 1$. The first term of eqn (3) is the size broadening while the second term describes broadening due to strain. The coherence length D, can be estimated from peak widths
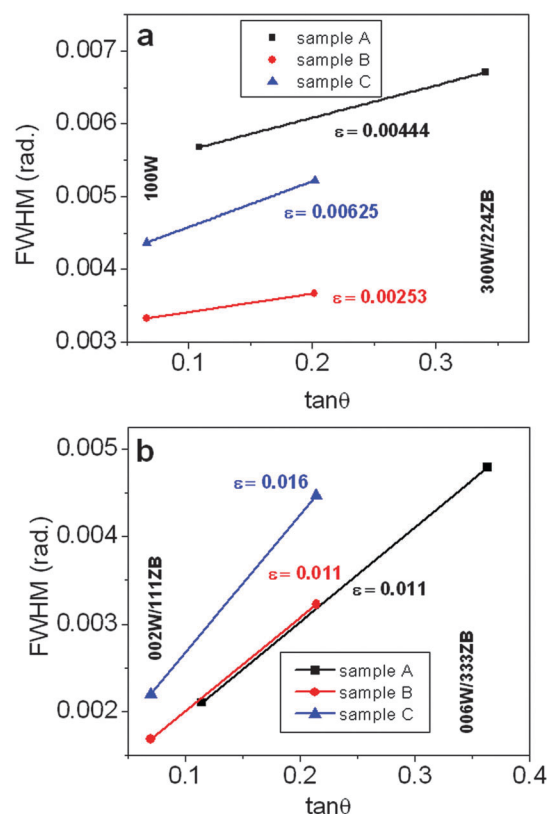
Table 2 FWHM (rad) and relative peak intensities of undoped and Mn^{2+}-doped CdSe NWs

|	Sample A		Sample B		Sample C		Sample D	
	FWHW		FWHW		FWHW		FWHW	
Peaks	(rad)	Relative intensity	(rad)	Relative intensity	(rad)	Relative intensity	(rad)	Relative intensity
100W	0.00568	0.38584	0.00332	0.53241	0.00437	0.31844		
002W/111ZB	0.00210	1.00000	0.00168	1.00000	0.00220	1.00000	0.00530	1.00000
101W	0.00701	0.21169	0.00398	0.26745	0.01845	0.26652		
110W/220ZB	0.00599	0.73681	0.00424	0.78189	0.00603	0.55022	0.01020	0.45688
103W	0.01215	0.09261	0.00797	0.23934	0.01494	0.18808		
112W/311ZB	0.00647	0.65164	0.00494	0.52760	0.00578	0.53010	0.01000	0.37073
203W	0.01083	0.17013	0.00650	0.12472	0.00932	0.07358		
210W	0.00684	0.15933	0.00453	0.13600	0.00247	0.06044		
211W/331ZB	0.00807	0.12955	0.00453	0.10953	0.00865	0.07041		
105W	0.01595	0.14676	0.00737	0.11409	0.02213	0.03977		
300W/224ZB	0.00671	0.24254	0.00366	0.23822	0.00522	0.15560		
213W	0.01113	0.23500	0.00579	0.17922	0.00693	0.12290		
006W/333ZB	0.00480	0.24700	0.00322	0.19673	0.00447	0.14259		
205W	0.01070	0.08542	0.00635	0.09091	0.00931	0.04882		
220W/044ZB	0.00618	0.12674	0.00376	0.15419	0.00565	0.08129		
222W	0.00667	0.25977	0.00471	0.23246	0.00530	0.17021		
312W	0.01357	0.09869	0.00660	0.11608	0.00743	0.06871		

of low q reflections. For the present estimate the very small instrumental peak width of few seconds of the arc is neglected. Perpendicular to the growth axis, the radial coherence length of the NW is estimated from the peak widths of 100W and 110W/220ZB peaks. Using the FWHM, listed in Table 2, D_{rad} = 12 nm for samples A and B and 8 nm for sample C, which is in reasonable agreement with the NW diameters extracted from TEM images (Table 1). On the other hand the coherence length along the growth direction, D_{axial}, is extracted from 002W/111ZB peak widths. This peak is always sharp and measures 32 nm for sample A and 30 nm for sample B but decreases to 22 nm for sample C and less than 10 nm for sample D (Table 2).

Whereas the peak width of higher order reflections such as 220W/044ZB differs moderately compared to 110W/220ZB, it increases by a factor of two for 006W/333ZB compared to 002W/111ZB. The changes in the peak width can be used to determine the impact of strain which is shown in Fig. 5a and b. The results for samples A, B and C follow eqn (3). In the radial direction the strain impact is less than 1% but it increases moderately with the increase of doping. In contrast along the axial direction the strain value increases rapidly and exceeds 1% for all samples. Note that this estimate was not performed for sample D due to the absence of high order reflections.

The shape of many reflections is affected by SFs and cannot be used for the Williams–Hall analysis. SF affected reflections are 103W, 203W, 105W, 205W, 210W, 211W, 213W, and 312W. They are always larger compared to the reflections which are not affected by SF, similar to our previous findings.[32] However, this defect broadening differs among the samples. Comparing the 101W and 105W reflections, for example, the peak widths of sample C always are larger compared to those measured for sample A. On the other hand sample B always shows smaller peak widths of SF sensitive reflections compared to sample A, confirming that moderate doping may induce higher crystal perfection.

Fig. 5 Strain analyses along (a) the axial direction and (b) the radial direction of undoped and Mn^{2+}-doped CdSe NWs.

In order to estimate the density and distribution of SF within the samples the peak broadening and relative peak intensities were simulated using the simulation packet DISCUS.[21] It simulates the powder diffraction patterns by means of a model structure of CdSe NWs. In simulation NWs
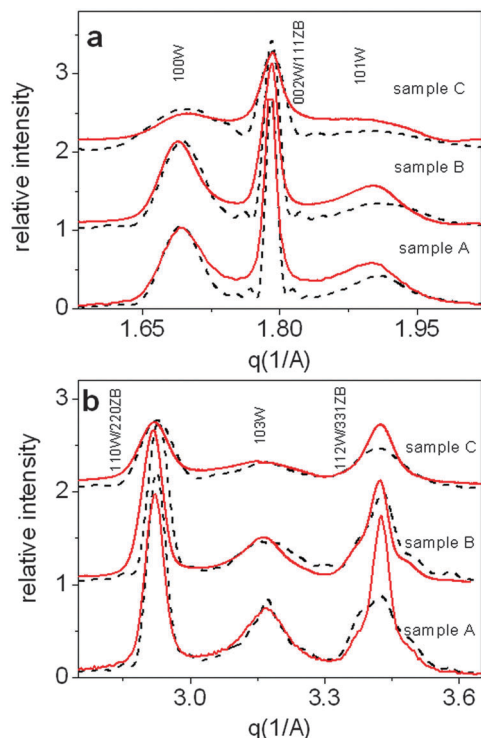
Fig. 6 Comparison between the simulated (dash curves) and experimental (solid curves) diffraction patterns of undoped and Mn^{2+}-doped CdSe NWs.

of a certain length were created using the lattice parameters, the mean NW diameter and the ZB content shown in Table 1 by stacking hexagonally dense packed layers of the measured NW diameter in W or ZB sequence including a certain distribution of SFs. The powder pattern was created by averaging over about 100 NWs calculated with the same number but different sequence of SFs. In Fig. 6 we show the results for samples A, B and C for two triples of reflections, 100W, 002W/111ZB and 101W (Fig. 6a) and 110W/220ZB, 103W and 112W (Fig. 6b). For samples A, B and C the NW length was calculated as 35 nm, 27 nm and 19 nm. SF parameters of sample A were taken as 5% growth fault and 15% deformation faults, for sample B 12% growth faults and 12% deformation faults and for sample C 16% deformation faults. The simulation fits the experimental data qualitatively correct. The normalized intensity of the simulated pattern is slightly different from the intensity found in the experiment but the FWHM are qualitatively correctly described. As in the experiment the 002W/111ZB reflection is the dominant one. It also confirms the similarity of samples A and B and the deterioration of sample C measured by decreasing peak intensities and increasing peak widths compared to samples A and B. Also the increase in FWHM of the SF affected peaks, such as 101W and 103W are reflected. Major discrepancies appear at the 112W/331ZB peak probably caused by strain effects which were not considered in simulation. As in the experiment sample B is revealed as more perfect compared to sample A (undoped) when a smaller number of SFs are considered. This is in agreement with the lower strain. In contrast sample C is worse than sample A. These results suggest that the

introduction of Mn^{2+} into the CdSe lattice can improve or deteriorate their crystal structure, depending on the dopant concentration.

Conclusions

In summary, powder X-ray diffraction was used to quantify the structural parameters of Mn^{2+}-doped CdSe NWs grown by the SLS method. A detailed analysis of the structural properties shows that all doped NWs exhibit a mixture of W and ZB crystal structures as found for the undoped sample where the relative ZB contribution increases as a function of doping concentration. This is accompanied by an increasing number of SFs. The comparison of simulated XRD patterns with the experimental data shows that the increase in Mn^{2+} concentration in CdSe NWs increases the stacking faults. The diameters of the NWs from the XRD measurement are in good agreement with the TEM results. The strain and coherence length are also dependent on the dopant and are extracted from the Williamson Hall relation. The doping of Mn^{2+} into CdSe NWs is anisotropic and preferentially affects the 002 facet more than the 110 facet while increasing the surface energy and in turn contribute to strain. Our results provide experimental evidence on the importance of deliberate control of doping level in NWs. Depending on the doping level host crystallinity can be improved or deteriorated. In the present case the crystallinity was optimum at a low Mn^{2+} concentration but degraded for a higher doping level. Therefore our results might serve as a shuttling pad for future optimization of doping.

Notes and references

1 Y. N. Xia, P. D. Yang, Y. G. Sun, Y. Y. Wu, B. Mayers, B. Gates, Y. D. Yin, F. Kim and Y. Q. Yan, *Adv. Mater.*, 2003, **15**, 353–389.
2 P. Yang, R. Yan and M. Fardy, *Nano Lett.*, 2010, **10**, 1529–1536.
3 Z. Li, Q. Sun, X. D. Yao, Z. H. Zhu and G. Q. M. Lu, *J. Mater. Chem.*, 2012, **22**, 22821–22831.
4 D. J. Norris, A. L. Efros and S. C. Erwin, *Science*, 2008, **319**, 1776–1779.
5 M. Y. Bashouti, R. T. Tung and H. Haick, *Small*, 2009, **5**, 2761–2769.
6 Y. Paska, T. Stelzner, S. Christiansen and H. Haick, *ACS Nano*, 2011, **7**, 5620–5626.
7 Y. Paska, T. Stelzner, O. Assad, U. Tisch, S. Christiansen and H. Haick, *ACS Nano*, 2012, **6**, 335–345.
8 X. Hu, G. Li and J. C. Yu, *Langmuir*, 2009, **26**, 3031–3039.
9 M. Dahan, T. Laurence, F. Pinaud, D. S. Chemla, A. P. Alivisatos, M. Sauer and S. Weiss, *Opt. Lett.*, 2001, **26**, 825–827.
10 C. C. Chen, Y. J. Hsu, Y. F. Lin and S. Y. Lu, *J. Phys. Chem. C*, 2008, **112**, 17964–17968.
11 S. A. Wolf, D. D. Awschalom, R. A. Buhrman, J. M. Daughton, S. von Molnar, M. L. Roukes, A. Y. Chtchelkanova and D. M. Treger, *Science*, 2001, **294**, 1488–1495.

12 R. Beaulac, P. I. Archer and D. R. Gamelin, *J. Solid State Chem.*, 2008, **181**, 1582–1589.

13 P. I. Archer, S. A. Santangelo and D. R. Gamelin, *Nano Lett.*, 2007, **7**, 1037–1043.

14 V. I. Klimov, A. A. Mikhailovsky, S. Xu, A. Malko, J. A. Hollingsworth, C. A. Leatherdale, H. J. Eisler and M. G. Bawendi, *Science*, 2000, **290**, 314–317.

15 V. V. Protasenko, K. L. Hull and M. Kuno, *Adv. Mater.*, 2005, **17**, 2942–2949.

16 A. Myalitsin, C. Strelow, Z. Wang, Z. Li, T. Kipp and A. Mews, *ACS Nano*, 2011, **5**, 7920–7927.

17 Z. Li, A. J. Du, Q. Sun, M. Aljada, L. N. Cheng, Z. H. Zhu, M. J. Riley, Z. X. Cheng, X. L. Wang, J. Hall, E. Krausz, S. Z. Qiao, S. C. Smith and G. Q. Lu, *Chem. Commun.*, 2011, **47**, 11894–11896.

18 Z. Li, X. Ma, Q. Sun, Z. Wang, J. Liu, Z. Zhu, S. Z. Qiao, S. C. Smith, G. M. Lu and A. Mews, *Eur. J. Inorg. Chem.*, 2010, 4325–4331.

19 Z. Li, A. J. Du, Q. Sun, M. Aljada, Z. H. Zhu and G. Q. Lu, *Nanoscale*, 2012, **4**, 1263–1266.

20 J. H. Yu, X. Y. Liu, K. E. Kweon, J. Joo, J. Park, K. T. Ko, D. Lee, S. P. Shen, K. Tivakornsasithorn, J. S. Son, J. H. Park, Y. W. Kim, G. S. Hwang, M. Dobrowolska, J. K. Furdyna and T. Hyeon, *Nat. Mater.*, 2010, **9**, 47–53.

21 *Diffuse Scattering and Defect Structure Simulations: A Cook Book Using the Program DISCUS*, ed. R. B. Neder and T. Proffen, Oxford University Press, USA, 2008.

22 F. D. Wang, A. G. Dong, J. W. Sun, R. Tang, H. Yu and W. E. Buhro, *Inorg. Chem.*, 2006, **45**, 7511–7521.

23 M. Kuno, *Phys. Chem. Chem. Phys.*, 2008, **10**, 620–639.

24 Z. Li, A. Kornowski, A. Myalitsin and A. Mews, *Small*, 2008, **4**, 1698–1702.

25 Z. Li, Ö. Kurtulus, F. Nan, A. Myalitsin, Z. Wang, A. Kornowski, U. Pietsch and A. Mews, *Adv. Funct. Mater.*, 2009, **19**, 3650–3661.

26 Z. Li, L. N. Cheng, Q. Sun, Z. H. Zhu, M. J. Riley, M. Aljada, Z. X. Cheng, X. L. Wang, G. R. Hanson, S. Z. Qiao, S. C. Smith and G. Q. Lu, *Angew. Chem., Int. Ed.*, 2010, **49**, 2777–2781.

27 Z. Wang, Z. Li, A. Kornowski, X. D. Ma, A. Myalitsin and A. Mews, *Small*, 2011, **7**, 2464–2468.

28 A. Biermanns, S. Breuer, A. Davydok, L. Geelhaar and U. Pietsch, *J. Appl. Crystallogr.*, 2012, **45**, 239–244.

29 A. Diaz, C. Mocuta, J. Stangl, B. Mandl, C. David, J. Vila-Comamala, V. Chamard, T. H. Metzger and G. Bauer, *Phys. Rev. B: Condens. Matter Mater. Phys.*, 2009, **79**, 125324.

30 A. Biermanns, A. Davydok, H. Paetzelt, A. Diaz, V. Gottschalch, T. H. Metzger and U. Pietsch, *J. Synchrotron Radiat.*, 2009, **16**, 796–802.

31 G. M. Dalpian and J. R. Chelikowsky, *Phys. Rev. Lett.*, 2006, **96**, 226802.

32 O. Kurtulus, Z. Li, A. Mews and U. Pietsch, *Phys. Status Solidi A*, 2009, **206**, 1752–1756.

33 S. Kar, S. Santra and H. Heinrich, *J. Phys. Chem. C*, 2008, **112**, 4036–4041.

34 S. H. Wei and S. B. Zhang, *Phys. Rev. B: Condens. Matter Mater. Phys.*, 2000, **62**, 6944–6947.

35 N. Karar, F. Singh and B. R. Mehta, *J. Appl. Phys.*, 2004, **95**, 656–660.

36 *X-Ray Diffraction*, ed. B. E. Warren, Dover Publications, 1990.

37 G. K. Williamson and W. H. Hall, *Acta Metall.*, 1953, **1**, 22–31.

38 S. Dhara and P. K. Giri, *J. Nanosci. Nanotechnol.*, 2011, **11**, 9215–9221.

39 R. Viswanatha, S. Sapra, S. Sen Gupta, B. Satpati, P. V. Satyam, B. N. Dev and D. D. Sarma, *J. Phys. Chem. B*, 2004, **108**, 6303–6310.